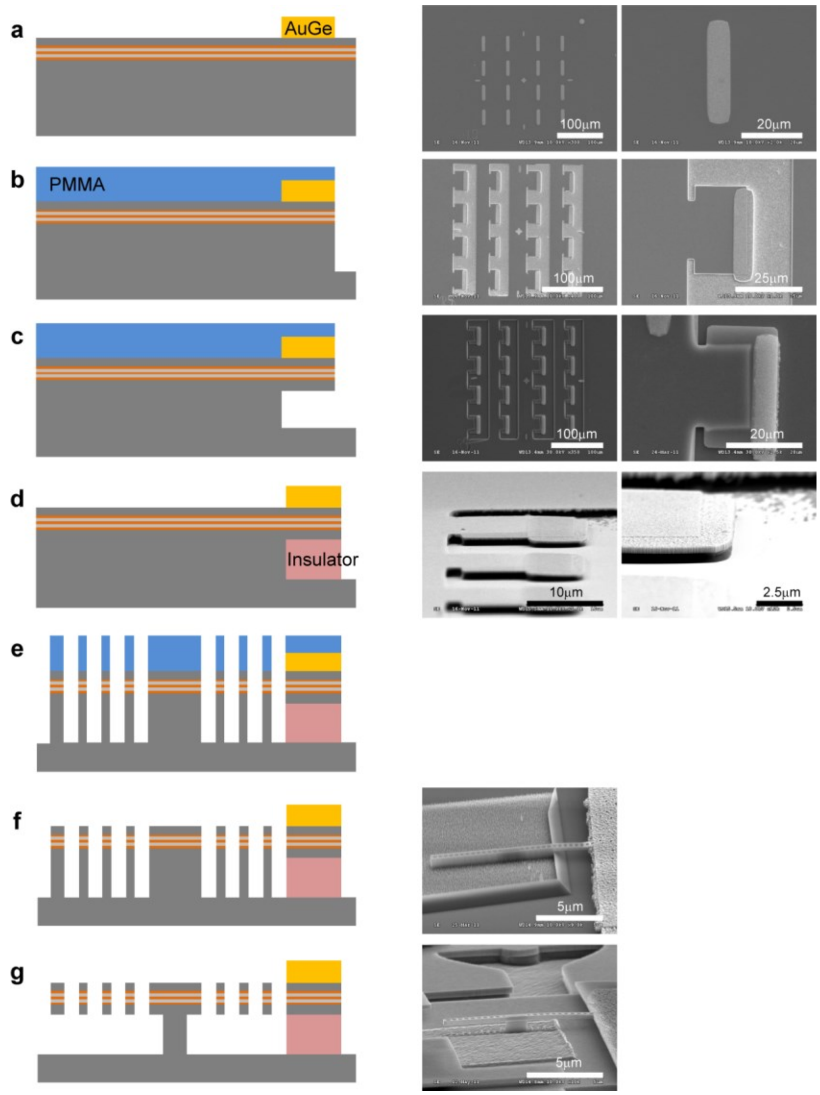

Supplementary Figure S1 | Device fabrication. Schematic illustrations (left column) and SEM images (right column) of the fabrication procedure for the nanobeam lasers. **a,** The 100-nm-thick AuGe *n*-contact electrode is deposited on the InGaAsP/InP wafer using a thermal evaporator. The electrode is then annealed at 250°C for 10 minutes in a vacuum chamber for ohmic contact. **b,** A mesa pattern including the electrode is formed using electron-beam lithography and chemically-assisted ion-beam etching (CAIBE). **c,** The InP sacrificial layer underneath the InGaAsP slab and *n*-electrode is partially removed by selective wet etching using HCl solution at room temperature. **d,** The residual polymethylmethacrylate (PMMA) layer on top of the InGaAsP slab is removed by O_2 plasma and then, the wet-etched region is filled with a dielectric material for mechanical stability. **e,** A nanobeam structure is defined using aligned electron-beam lithography and CAIBE. **f,** The residual PMMA layer is removed by O_2 plasma. **g,** The submicron-sized central post is delicately fabricated by time-controlled selective wet etching using diluted HCl solution ($HCl:H_2O$ = 3:1) at 10°C.

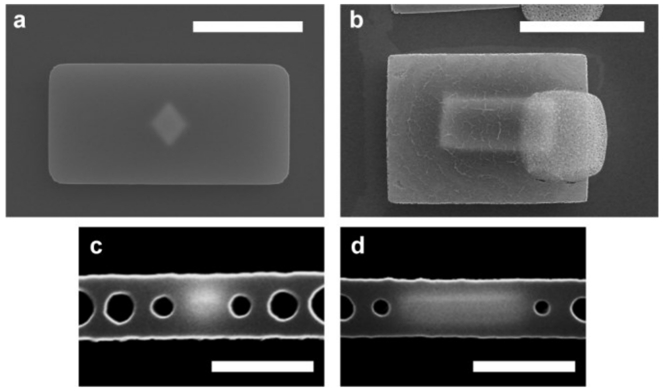

Supplementary Figure S2 | Anisotropic wet etching characteristics of the InP sacrificial layer. a and **b,** Anisotropic wet etching profiles of a central InP post are shown underneath the rectangular-shaped InGaAsP slab. A rhombus-shaped InP post is formed when the slab is defined along the <110> direction (**a**), whereas a rectangular-shaped post is formed when the slab is defined along the <100> direction (**b**). The scale bars in **a** and **b** are 10 μm. **c** and **d**, SEM images of (**c**) fabricated single-cell and (**d**) three-cell nanobeam structures. The formation of submicron-sized posts is highly controllable due to anisotropic wet etching characteristic of the InP sacrificial layer. The scale bars in **c** and **d** are 1 μm.

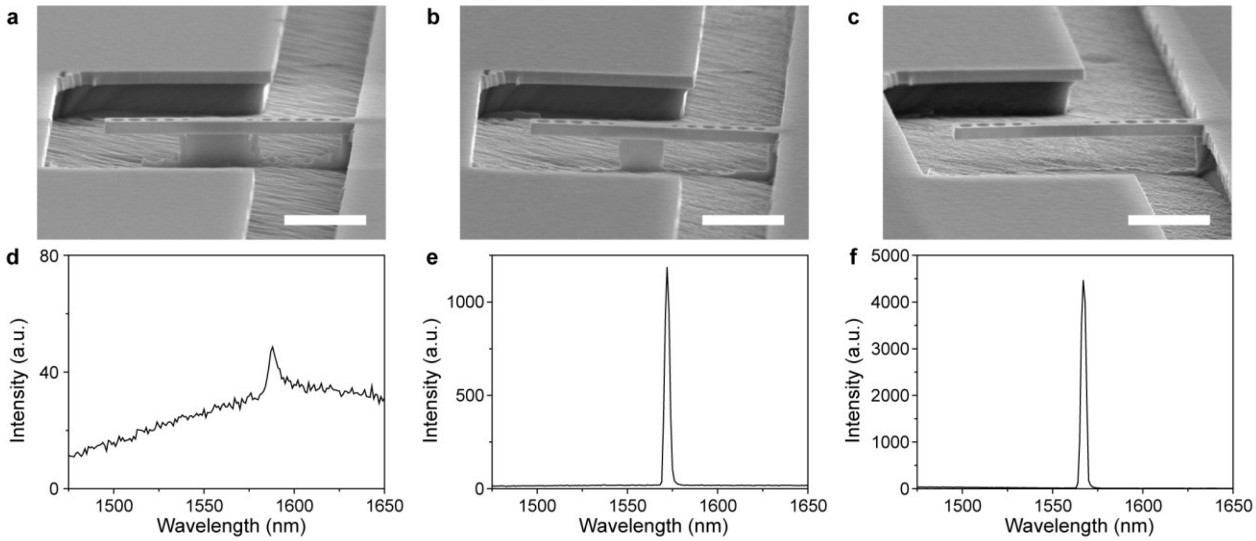

Supplementary Figure S3 | Post-size-dependent photoluminescence spectra. a–c, Tilted-view SEM images of three-cell nanobeam structures with three different post sizes. The post size decreases gradually with increasing wet etching time. The post is removed completely in **c**. The scale bars in **a–c** are 2 μm. **d–f**, Measured photoluminescence (PL) spectra from the nanobeam structures of **a–c**. Lasing actions are observed in the nanobeam structures with a submicron-sized post and no post in **e** and **f**, respectively. The estimated *Q* factors are (**a**) 100, (**b**) 1,500, and (**c**) 1,900, respectively, through contour FDTD computation.

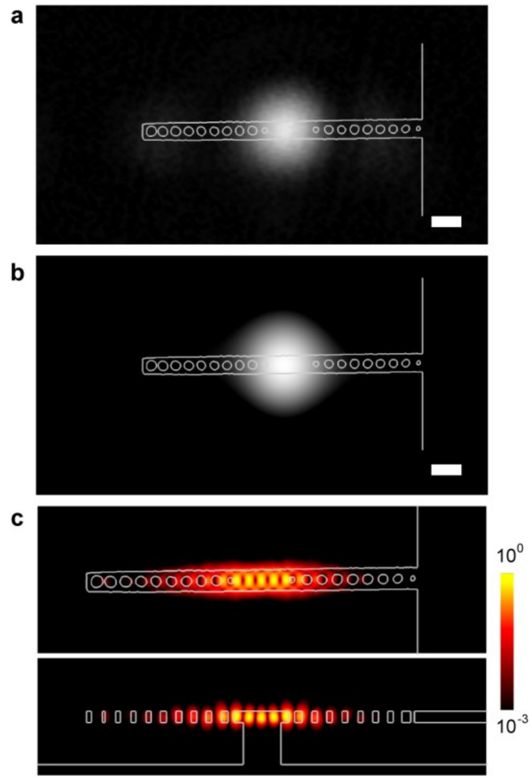

Supplementary Figure S4 | Measured and calculated mode images in a three-cell nanobeam laser. a, Lasing mode profile captured by an IR camera. **b,** Calculated vertical component of time-averaged Poynting vector distribution at a position 3.6 μm above the slab, which represents those propagating photons that have escaped from the bound mode shown in **c**. The scale bars in **a** and **b** are 1 μm. **c,** Top and side views of the calculated electric field intensity distribution, log $|E|^2$. The SEM image of Fig. 4a is used for this simulation. The resonant wavelength of the mode is 1,560 nm. Its *Q* factor and mode volume are ~1,500 and $0.56(\lambda/n)^3$, respectively.

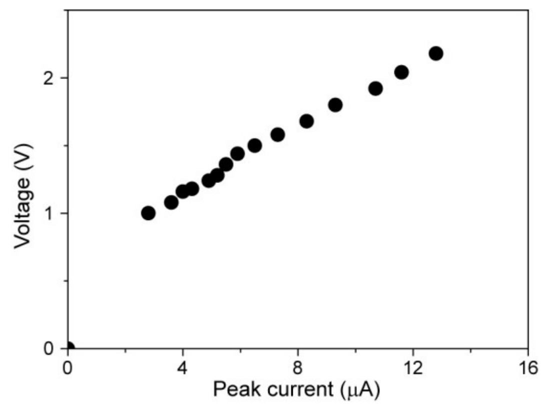

Supplementary Figure S5 | Measured peak voltage versus peak current curve in a three-cell nanobeam laser. The electrical resistance is ~120 kΩ and the voltage at threshold is 1.4 V. Further study will be necessary to analyze the resistances of the contact pad, n-side nanobeam and p-side post, separately.

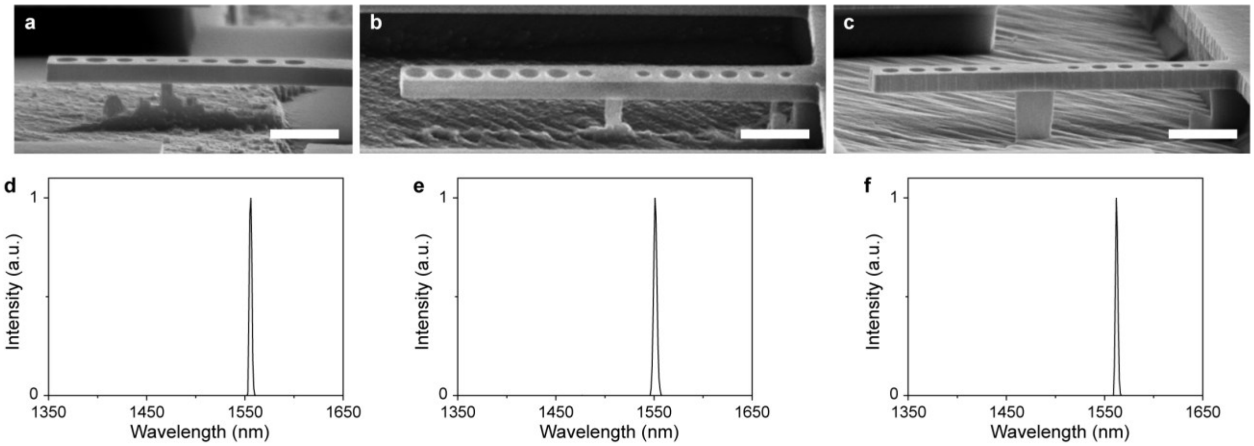

Supplementary Figure S6 | Optically pumped nanobeam lasers. a–c, Tilted views of SEM images of (**a**) zero-cell, (**b**) single-cell, and (**c**) two-cell nanobeam structures. In each cavity, a submicron-sized central post is formed underneath the cavity. The scale bars in **a–c** are 1 μm. **d–f**, Lasing spectra measured from (**d**) zero-cell, (**e**) single-cell, and (**f**) two-cell nanobeam structures by optical pumping. Single-mode lasing actions are observed in all cavities. The estimated *Q* factors are (**a**) 460, (**b**) 510, and (**c**) 730, respectively, through contour FDTD computation.

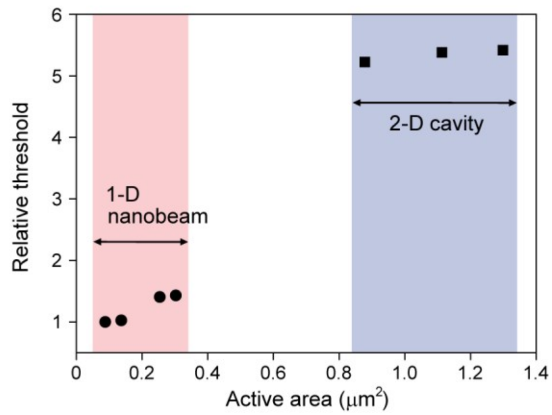

Supplementary Figure S7 | Analysis of lasing thresholds. Relative threshold plotted as a function of active area that is changed by air hole radius, with the assumption of material parameters used in Ref. 32. Main parameters are as follows: *Q* factor 1500, gain coefficient 1500 cm^{-1}, surface recombination velocity 1.0×10^{4} cm/s, bimolecular radiative coefficient 1.6×10^{-10} cm^{3}/s, Auger coefficient 5.0×10^{-29} cm^{6}/s, and transparent carrier density 1.5×10^{18} cm^{-3}. The 2-D cavity consists of triangular-lattice photonic crystal patterns with the same structural parameters as the 1-D nanobeam cavity (the lattice constant *a* is 370 nm). We considered only the area within the carrier diffusion length. As a result of a simple rate equation including nonradiative surface recombination, the threshold of the 1-D nanobeam laser is ~5.5 times lower than that of 2-D photonic crystal laser.

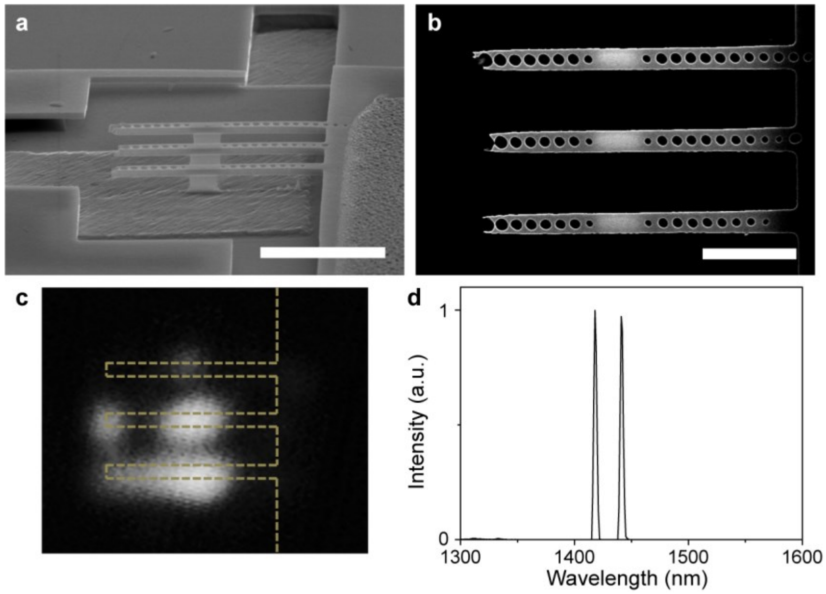

Supplementary Figure S8 | Nanobeam laser array. a and **b,** (**a**) Tilted and (**b**) top views of SEM images of an electrically driven nanobeam laser array comprising three parallel three-cell nanobeam structures connected to a common *n*-electrode. Submicron-sized central posts are formed in the three nanobeam structures. The scale bars in **a** and **b** are 2.5 and 5 μm, respectively. **c**, Lasing mode image from the nanobeam laser array, which is captured by an IR camera. The nanobeam array in **b** is superimposed on the image as the dotted line. Strong lasing emission is observed from the middle and bottom nanobeams, while the emission from the top nanobeam is relatively weak. **d**, Measured lasing spectrum from the nanobeam array at a peak current of 260 μA.